

Revisiting 2D Numerical Models for the 19th century outbursts of η Carinae

R.F. González^{1*}, A.M. Villa¹, G.C. Gómez¹, E.M. de Gouveia Dal Pino²,
A.C. Raga³, J. Cantó⁴, P.F. Velázquez³, E. de la Fuente⁵

¹Centro de Radioastronomía y Astrofísica (UNAM), Ap.Postal 3-72, C.P.: 58190, Morelia, Michoacán, México

²Instituto Astronômico e Geofísico (USP), R. do Matão 1226, 05508-090 São Paulo, SP, Brasil

³Instituto de Ciencias Nucleares (UNAM), Ap.Postal 70-543, CP: 04510, México D.F., México

⁴Instituto de Astronomía (UNAM), Ap.Postal 70-264, CP: 04510, México D.F., México

⁵Departamento de Física, CUCEI, Universidad de Guadalajara, Avenida Revolución SN, Guadalajara, Jalisco, México

Accepted —. Received —;

ABSTRACT

We present here new results of two-dimensional hydrodynamical simulations of the eruptive events of the 1840s (the great) and the 1890s (the minor) eruptions suffered by the massive star η Car. The two bipolar nebulae commonly known as the Homunculus and the little Homunculus were formed from the interaction of these eruptive events with the underlying stellar wind. As in previous work (Gonzalez et al. 2004a, 2004b), we assume here an interacting, nonspherical multiple-phase wind scenario to explain the shape and the kinematics of both Homunculi, but adopt a more realistic parametrization of the phases of the wind. During the 1890s eruptive event, the outflow speed *decreased* for a short period of time. This fact suggests that the little Homunculus is formed when the eruption ends, from the impact of the post-outburst η Car wind (that follows the 1890s event) with the eruptive flow (rather than by the collision of the eruptive flow with the pre-outburst wind, as claimed in previous models; Gonzalez et al. 2004a, 2004b). Our simulations reproduce quite well the shape and the observed expansion speed of the large Homunculus. The little Homunculus (which is embedded within the large Homunculus) becomes Rayleigh-Taylor unstable and develop filamentary structures that resembles the spatial features observed in the polar caps. In addition, we find that the interior cavity between the two Homunculi is partially filled by material that is expelled during the decades following the great eruption. This result may be connected with the observed double-shell structure in the polar lobes of the η Car nebula. Finally, as in previous work, we find the formation of tenuous, equatorial, high-speed features that seem to be related to the observed equatorial skirt of η Car.

Key words: stars: individual (η Carinae) — stars: winds, outflows — hydrodynamics — shock waves

1 INTRODUCTION

Located at a distance of 2.3 kpc, one of the most massive stars in our Galaxy ever discovered, η Car is a well-known example of the evolved and unstable luminous blue variable (LBV) stars, characterized by sporadic, violent mass-loss eruptive events (e.g., Humphreys & Davidson 1994). The 19th century spectrograms of η Car (see also Walborn & Liller 1977; Humphreys, Davidson & Smith 1999 and references therein) provide evidence that the star underwent a giant eruption during ~ 20 yr around the 1840s, where a few

solar masses of gas ($\geq 10 M_{\odot}$) were expelled into the interstellar medium, and the total luminous output of $\sim 10^{49.5}$ – $\sim 10^{50}$ erg was comparable to a supernova explosion (Smith et al. 2003a). It is still not understood how and why this outburst occurred, but it may be connected with η Car being a binary star system (e.g., Daminieli 1996; Daminieli, Conti, & Lopes 1997). From this event, a symmetric, bipolar nebula known as the “Homunculus” (that extends from -8 to $+8$ arcsec along its major axis) was produced (Humphreys & Davidson 1994; Currie et al. 1996; Davidson & Humphreys 1997; Smith & Gehrz 1998). During the 1890s, the historical light curve of η Car also shows a much fainter eruptive event of shorter duration (~ 10 yr), but still an outburst in the

* E-mail: rf.gonzalez@astrosmo.unam.mx

sense that the mass loss rate was enhanced compared with the normal underlying wind. This eruption resulted in the formation of a smaller nebula embedded within the large Homunculus (with an angular size of about ± 2 arcsec) called the “Little Homunculus” (LH) (Ishibashi et al. 2003; Smith 2005). With a total mass of $\sim 0.1 M_{\odot}$, the polar caps of the LH currently move at slower speeds ($\sim 250 \text{ km s}^{-1}$) than the large Homunculus in the polar direction ($\sim 650 \text{ km s}^{-1}$), but shares the same prolate geometry. The total kinetic energy released in the 1890s event is $\sim 10^{46.5}$ erg (a factor of $\sim 10^3$ smaller than the kinetic energy expelled during the great eruption). Apart from both Homunculi, observations of η Car with the Hubble Space Telescope (e.g., Morse et al. 1998) also show the presence of an equatorial skirt (orthogonal to the axis of the Homunculus) that moves with velocities of $100\text{--}350 \text{ km s}^{-1}$ (Smith & Gehrz 1998; Davidson et al. 2001), although high speed features, with typical velocities of $\sim 750 \text{ km s}^{-1}$ (Smith et al. 2003b) or even larger (Weis 2005) have also been detected. These equatorial components may have been expelled from both the 1840s and the 1890s outbursts (e.g., Davidson & Humphreys 1997). The large Homunculus is the central portion of a larger nebula (the outer ejecta) around η Car that extends up to a diameter of 60 arcsec (e.g., Weis 2001, 2005; Walborn 1976; Walborn et al. 1978). The outer ejecta are not symmetric and contain numerous filaments and knots that may have been produced by previous stellar wind mass loss. The sizes and morphology of such structures in the outer ejecta are manifold. Radial velocities for the knots reach up to 2000 km s^{-1} (Weis 2001, Weis 2005), but the average expansion velocity of the outer ejecta lies at lower values (around 750 km s^{-1}), similar to the speeds found in the Homunculus. The outer ejecta also follow a bipolar pattern, like the large Homunculus, with approximately the same axis of symmetry.

At optical wavelengths, the large Homunculus is mainly a reflection nebula. Its spectrum shows the presence of dust scattered emission (e.g., Hillier & Allen 1992) that allows one to see indirectly the shape of the η Car wind (see Smith et al. 2003b) and also low-excitation intrinsic emission. In addition, near-infrared spectra obtained by Smith (2006) confirmed the existence of a double-shell structure at the edges of the polar lobes of the Homunculus (which was previously inferred from thermal dust emission; see Smith et al. 2003a). A thin outer shell of intrinsic H_2 emission (that traces the main scattering layer seen in visual images), and a thicker inner skin of [Fe II] (which partially fills the interior of the lobes). On the other hand, the outer ejecta are an emission nebula. Smith & Morse (2004) present optical spectra of η Car showing strong oxygen lines in some emission features of the outer ejecta. At high energies, Chandra has detected X-ray emission from the large-scale nebula around the star (and also from the central object, probably due to a wind collision region around the massive binary system; e.g., Corcoran et al. 2001; Pittard & Corcoran 2002). Soft X-ray (0.1–0.8 keV) observations by Seward et al. (2001) show an extended shell clearly associated with the debris field of the outer ejecta which are compatible with a collision process between a fast wind and cometary knots of slower material. The η Car nebula is also a bright radio source consistent with thermal (free-free) emission. Observations by Retallack (1983) at 1.415 GHz (taken with the Fleurs synthesis telescope) show emission from an overall region as large as 40

arcsec (i.e., larger than the optical Homunculus). González et al. (2006) estimated the contribution by shocks to the total radio-continuum emission detected from the η Car nebula. Using observational estimates of the wind parameters of the eruptive event of the 1890s and of the stellar wind after the end of the eruption, these authors investigated the evolution of the polar caps of the LH formed as a result of the collision between these outflows. They found that the LH emits continuum radiation which is detectable at radio wavelengths and indeed, has an appreciable contribution to the total flux of the η Car nebula.

Different models have been proposed to explain the shaping and kinematics of the η Car bipolar nebulae (see, for instance, Soker 2001; Soker 2004; Matt & Balick 2004; Gonzalez et al. 2004a, b; A. Frank et al. 1995, 1998). One possible explanation is that it is produced by the interaction of the winds expelled by the central star at different injection velocities (e.g., Icke 1988; Frank, Balick & Davidson 1995; Dwarkadas & Balick 1998; Frank, Ryu & Davidson 1998; Langer, García-Segura & Mac Low 1999; González et al. 2004a,b). Adopting a colliding wind scenario, González et al. (2004a,b) performed two-dimensional numerical simulations of the Homunculi nebulae of η Car. In their models, the large Homunculus is formed by the interaction of the eruptive outflow of the 1840s with the pre-outburst η Car wind (both with different degrees of nonspherical symmetry). A second eruption (assumed to be spherical) collides with the pre-outburst wind giving rise to the LH. These authors showed that such a scenario could explain the shape and kinematics of the Homunculi, and also the existence of the high-velocity features observed in the equatorial plane. However, their prescribed conditions to create the LH nebula do not agree with overall results suggest by the observations. During the 1890s event, the η Car wind slowed down and increased its mass loss rate, returning to its normal quiescent state after the eruption ended. Another observational result (as mentioned earlier) is that the Homunculus contains much more mass than that that had been previously recognized (Smith et al. 2003a). In this work, we perform new numerical simulations that incorporate these observational results and investigate the overall evolution of the bipolar outflows of η Car.

The paper is organized as follows. In § 2, we describe the model. The numerical simulations and the discussion of the results are presented in § 3, and in § 4 we draw our conclusions.

2 THE MODEL

In our model, we consider (see also González et al. 2004a,b) a simplified interacting wind scenario, in which a nonspherical outburst collides with a slow wind also with asymmetric density and velocity distributions. We suppose that η Car originated a nonspherical environment (prior to the major eruption of the 1840s) from the ejection of a pre-outburst wind into a homogeneous ambient medium. According to observational estimates, we also assume that both the mass loss rate and the injection velocity were drastically increased during the main eruption of the 1840s, after which the original slow wind resumes. We also suppose that the wind parameters are suddenly changed during the smaller mass-

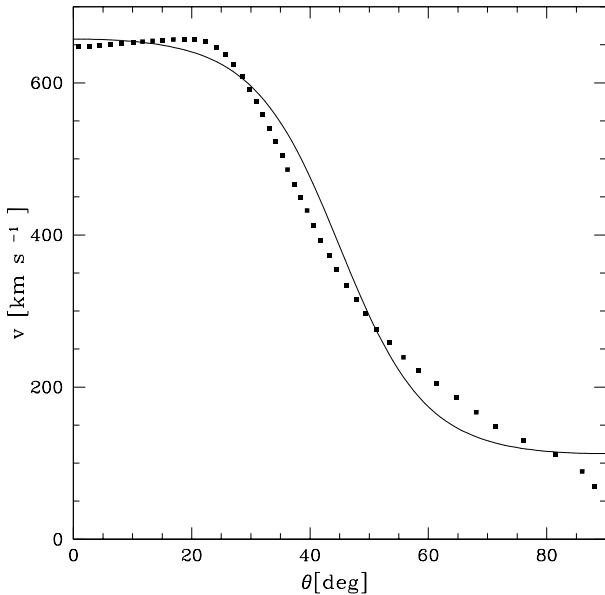


Figure 1. The solid line gives the best fitting curve to the measured velocity in H_2 (squares) by Smith (2006) at different latitudes of the η Car Homunculus (with $\theta = 0^\circ$ at the pole). For this fitting we have assumed $\lambda = 1.9$, $v_1 = 670 \text{ km s}^{-1}$, $v_2 = 100 \text{ km s}^{-1}$, which gives (see eq. [1]) a polar expansion velocity $v_p = 657.53 \text{ km s}^{-1}$ and $v_e = 112.47 \text{ km s}^{-1}$ at equator.

ejection event of the 1890s, after which the original wind again resumes. However, observations of η Car at this epoch (e.g. Whitney 1952; Walborn & Liller 1977) give evidence that the expansion speed of the stellar wind decreased during this eruption, rather than increasing (see also Le Sueur 1870). Such variabilities in the wind parameters of η Car during the 19th century outbursts must have resulted in the formation of a pair of double-shock wave structures (called working surfaces; see Raga et al. 1990), that correspond - in our colliding wind scenario - to the large and little Homunculi. Then, the large Homunculus would be produced by the interaction between an outburst wind (with a latitude-dependent velocity and density) and a pre-eruptive slower wind (also with a nonspherical symmetry). Nevertheless, the little Homunculus would be formed - unlike previous numerical modeling (González et al. 2004a,b) - from the impact of the post-outburst wind with the outflow expelled during the minor event, that is, when the eruption ended. According to González et al. (2006), a sudden increase in the ejection velocity at the end of the eruption instantaneously occurs and forms the inner nebula at the base of the wind (as the fast upstream flow begins to be ejected).

In order to estimate the flow parameters (such as the injection velocity v and the number density n) for the different wind phases, we have fitted a curve to the expansion speed of the outer H_2 shell of the η Car Homunculus measured by Smith (2006). From this fitting, we find a latitude-dependent velocity given by,

$$v = v_1 F(\theta), \quad (1)$$

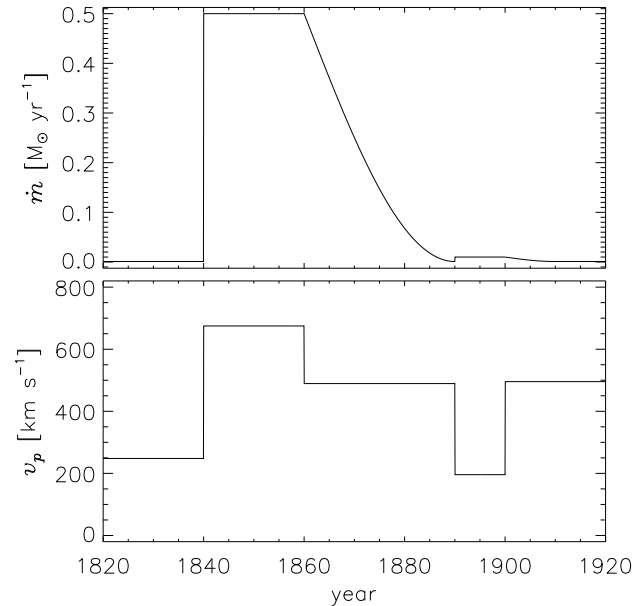


Figure 2. Behaviour of the adopted parameters of the interacting outflows. We show the mass loss rate (top panel) and the wind velocity at the poles (bottom panel) as functions of time. During the great eruption of the 1840s (~ 20 yr), both parameters were suddenly increased, while during the minor event of the 1890s the flow velocity decreased for ~ 10 yr. In addition, we assume a gradual fading in the mass loss rate during the years after the end of both events, asymptotically approaching the mass loss rate of the underlying wind ($10^{-3} M_\odot \text{ yr}^{-1}$).

with

$$F(\theta) = \frac{(v_2/v_1) + e^{2z}}{1 + e^{2z}},$$

where the parameter $z = \lambda \cos(2\theta)$ controls the shape of the Homunculus, λ is a constant and θ is the polar angle. The velocities v_1 and v_2 are related to the expansion speed in the polar ($\theta = 0^\circ$) and equatorial ($\theta = 90^\circ$) directions. In Figure 1, we present the best fit to Smith (2006)'s observations obtained with $\lambda = 1.9$, $v_1 = 670 \text{ km s}^{-1}$, $v_2 = 100 \text{ km s}^{-1}$. With these parameters, the predicted expansion velocity in the polar and equatorial directions are $v_p = 657.53 \text{ km s}^{-1}$ and $v_e = 112.47 \text{ km s}^{-1}$, respectively. Using this fit of the expansion velocity of the outer Homunculus, we estimate the flow parameters of the interacting winds as follows.

From a straightforward application of the formalism developed by Cantó et al. (2000) for outflows with time-dependent injection velocities (see also González & Cantó 2002; Cantó et al. 2005), we studied the dynamical evolution of the Homunculus. Let us first consider the downstream wind with latitude-dependent injection velocity v_0 (given by eq. [1]) and constant mass loss rate per unit solid angle. Then, the injection number density of the wind is equal to,

$$n = n_0 \left(\frac{r_0}{r} \right)^2 \frac{1}{F(\theta)}, \quad (2)$$

where $n_0 (= \dot{m}_0 / 4\pi\mu v_0 r_0^2)$; being μ the mean mass per nucleon and \dot{m}_0 the total mass loss rate) is the number density at the injection radius r_0 (assumed to be a few stellar radii).

TABLE 1

PARAMETERS OF THE COLLIDING OUTFLOWS

| Wind Phase | λ | v_1 [km s ⁻¹] | v_2 [km s ⁻¹] | v_p [km s ⁻¹] ($\theta = 0^\circ$) | v_e [km s ⁻¹] ($\theta = 90^\circ$) | \dot{m} [M _⊙ yr ⁻¹] |
|---------------------------|-----------|-----------------------------|-----------------------------|---|--|--|
| <i>Pre-outburst wind</i> | 2.4 | 250.00 | 14.00 | 248.07 | 15.93 | 10 ⁻³ |
| <i>Great Eruption</i> | 1.9 | 687.76 | 102.65 | 674.95 | 115.45 | 5 × 10 ⁻¹ |
| <i>Post-outburst wind</i> | 1.9 | 500.00 | 14.00 | 489.37 | 24.63 | 10 ⁻³ × $\phi(t)$ (†) |
| <i>Minor Eruption</i> | 1.9 | 200.00 | 10.00 | 195.84 | 14.16 | 10 ⁻² |
| <i>Post-outburst wind</i> | 1.9 | 500.00 | 300.00 | 495.62 | 304.38 | 10 ⁻³ × $\varphi(t)$ (‡) |

(†) see eq. [6]

(‡) see eq. [7]

Note that $F(\theta)$ depends on the particular values of v_1 , v_2 , and z of the pre-outburst wind.

When the great eruption begins, the wind parameters are suddenly increased to av_0 and $b\dot{m}_0$, respectively (where a and b are constants). Such a variation in the flow parameters forms instantaneously (at the base of the wind) a working surface (which will correspond in our model to the large Homunculus) that moves with a constant velocity given by,

$$v_{ws} = \sigma v_0, \quad (3)$$

with $\sigma = (a^{1/2} + ab^{1/2})/(a^{1/2} + b^{1/2})$. This velocity is intermediate between the low-velocity downstream wind (v_0) and the faster upstream outflow (av_0).

Given (for instance) v_0 and v_{ws} , equation (3) gives σ as a function of a and b . We estimate b from observations of the mass contained in the Homunculus and the duration of the major eruption (and compare with the mass loss rate of the standard wind of η Car) and then, we obtain a . Assuming the same latitude-dependent velocity and density (eqs. [1] and [2], respectively) for the pre-outburst wind and the great eruption, and using the fit to Smith (2006)'s observations of the expansion velocity of the η Car Homunculus (Fig. 1), we finally obtain the flow parameters at the different phases of the interacting winds, keeping v_0 as a free parameter.

The historical light curve of η Car shows a sudden increase in brightness when the eruptions of the 1840s and 1890s turned-on and a gradual fading during the years after the end of the eruptive events (e.g. Walborn & Liller 1977; Davidson 1987; Humphreys & Davidson 1994; Humphreys, Davidson & Smith 1999). This suggests that the post-outburst mass-loss rates of the major (\dot{m}_1) and the minor (\dot{m}_2) events decrease, approaching the mass loss rate of the underlying wind ($\dot{m}_0 = 10^{-3} \text{ M}_\odot \text{ yr}^{-1}$; e.g. Humphreys & Davidson 1994; Davidson & Humphreys 1997). We then consider,

$$\dot{m}_1 = \dot{m}_0 \phi(t), \quad (4)$$

and

$$\dot{m}_2 = \dot{m}_0 \varphi(t), \quad (5)$$

respectively, with

$$\phi(t) = \frac{\dot{m}_{ge}}{\dot{m}_0} + \left(1 - \frac{\dot{m}_{ge}}{\dot{m}_0}\right) \sin \left[\frac{\pi}{2} \left(\frac{t - t_1}{\Delta t_1} \right) \right], \quad (6)$$

and,

$$\varphi(t) = \frac{\dot{m}_{me}}{\dot{m}_0} + \left(1 - \frac{\dot{m}_{me}}{\dot{m}_0}\right) \sin \left[\frac{\pi}{2} \left(\frac{t - t_2}{\Delta t_2} \right) \right], \quad (7)$$

where $\dot{m}_{ge} (= 5 \times 10^{-1} \text{ M}_\odot \text{ yr}^{-1})$ and $\dot{m}_{me} (= 10^{-2} \text{ M}_\odot \text{ yr}^{-1})$ are the estimated mass loss rates during the eruptions, t_1 and t_2 correspond to the transition times when both events end, and $\Delta t_1 (= 30 \text{ yr})$ and $\Delta t_2 (= 10 \text{ yr})$ represent in our model the duration of the post-eruption phases. In Figure 2, we show the behaviour of the adopted parameters (the mass loss rate and the ejection velocity at the poles) of the interacting outflows as functions of time.

3 NUMERICAL SIMULATIONS

We have performed gasdynamic 2D numerical simulations (considering axial symmetry) of the 19th century outbursts of η Car. Adopting the colliding wind model described in §2, we use the adaptive-grid YGUAZÚ-A code originally developed by Raga et al. (2000; see also Raga et al. 2002) and modified by González et al. (2004a, b). This code integrates the hydrodynamic equations explicitly accounting for the radiative cooling with a set of continuity equations for the atomic/ionic species HI, HII, HeI, HeII, HeIII, CII, CIII, CIV, OI, OII, and OIII. The flux-vector splitting algorithm of Van Leer (1982) is employed. The simulations were computed on a five-level binary adaptive grid with a maximum resolution of $3.9 \times 10^{14} \text{ cm}$, corresponding to 1024×1024 grid points extending over a computational domain of $(4 \times 10^{17} \text{ cm}) \times (4 \times 10^{17} \text{ cm})$. The adopted abundances (by number) for the different elements are (H, He, C, O) = (0.9, 0.099, 0.0003, 0.0007).

3.1 Initial Physical conditions

In Table 1 (see also Fig. 2), we list the adopted parameters for the interacting winds. We have assumed different equator-to-pole velocity (and density) contrasts.

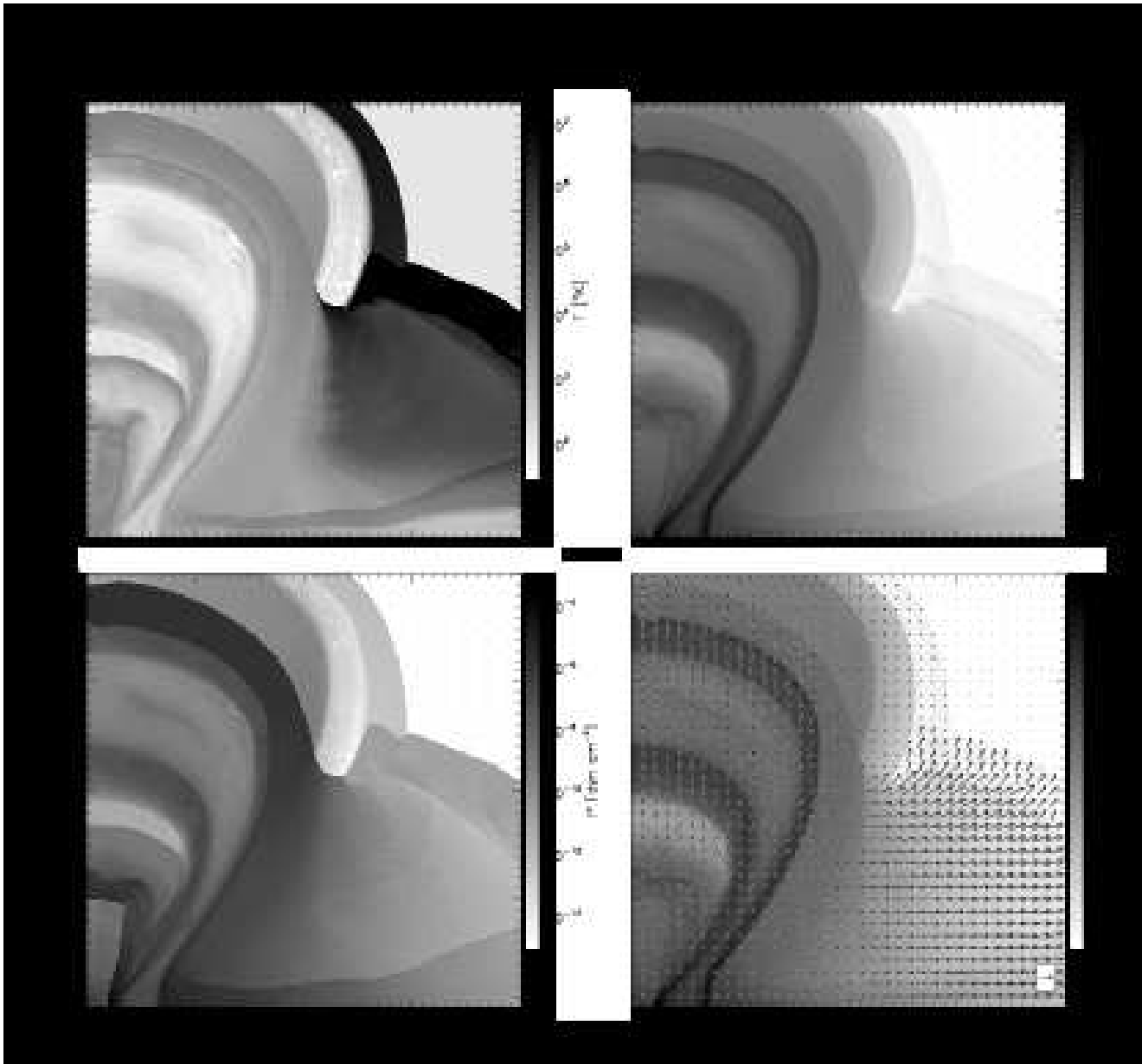


Figure 3. Stratifications of temperature (top left), density (top right), pressure (bottom left), and velocity-field superposed on the density map (bottom right) obtained 169 yr after the great eruption of η Car (i.e., around 2009) are presented. The arrow shown at the lower right corner of the velocity-field stratification corresponds to 1000 km s $^{-1}$ (see the text for more details)

Initially, the computational domain is filled by a homogeneous ambient medium with temperature $T_a = 10^2$ K and density $n_a = 10^{-3}$ cm $^{-3}$. Afterwards, a gaseous toroidal distribution is formed by the injection of a pre-outburst wind into this unperturbed environment (with a different λ parameter from the other injected later wind phases which controls the shape of the wind). For this wind, we have assumed a terminal velocity (in the polar direction) $v_1 = 248.07$ km s $^{-1}$ (González et al. 2004a,b) and a mass loss rate of 10^{-3} M $_{\odot}$ yr $^{-1}$ which was injected at a distance of $r_0 = 10^{16}$ cm (from the stellar surface) with a temperature of $T_0 = 10^4$ K. Once a poloidal environment is produced, a much faster ($= 674.95$ km s $^{-1}$) and massive outflow (5×10^{-1} M $_{\odot}$ yr $^{-1}$) is expelled during the estimated duration of the great

eruption (~ 20 yr; e.g. Davidson & Humphreys 1997). For this outburst phase (that dominates the momentum flux) we have adopted the same degree of nonspherical symmetry as the observed for the large Homunculus, as given in Figure 1. After this event, a third outflow (the post-outburst wind) is turned on with similar conditions to the current stellar wind of η Car (e.g. Le Sueur 1870; Smith et al. 2003b), that is, we assume an injection velocity of 489.37 km s $^{-1}$ at the poles and a time-dependent mass loss rate that approaches 10^{-3} M $_{\odot}$ yr $^{-1}$ (eqs. [4] and [6]). In order to account for the minor eruption, during 10 years (and 50 years after the great eruption event), we assumed a slower eruptive wind with a terminal velocity - along the symmetry axis - of ~ 195.84 km s $^{-1}$ and a mass loss rate of 10^{-2} M $_{\odot}$ yr $^{-1}$. After this

outflow, a faster ($= 495.62 \text{ km s}^{-1}$), but less massive wind with a mass loss rate approaching to $10^{-3} M_{\odot} \text{ yr}^{-1}$ (eqs. [5] and [7]) resumes. We also have assumed for this wind a higher speed ($= 304.38 \text{ km s}^{-1}$) at equator, which is consistent with the present-day latitudinal structure in η Car's stellar wind (Smith et al. 2003b).

We should notice that Smith (2006) calculated the mass loss distribution assuming uniform density as a function of latitude with a constant width. These are not the assumptions of our current models. Instead, we assumed that both the ejection velocity and the injection density depend on latitude (eqs. [1] and [2], respectively) and therefore, a constant mass loss rate per unit solid angle is adopted (see §2). However, a similar scenario to the Smith's findings was previously study in Gonzalez et al. (2004b), where we assumed a nonspherical outburst wind of the 1840s impinging on a slow pre-outburst wind with a larger mass-loss rate in the polar direction (run D). We found that this scenario does not develop significant equatorial features.

3.2 Results of the simulations

In this section we present the two-dimensional hydrodynamical numerical simulations performed for the outbursts of η Car, adopting the colliding wind scenario described in § 2. Figure 3 shows the temperature, density, pressure, and velocity maps computed for the interaction of the five winds above at a time $t = 169$ yr of evolution after the great eruption. As predicted in §2, the simulations show the formation of the outer Homunculus with a double-shock structure, having an inner shock that decelerates the fast outburst flow and an outer shock that accelerates the lower velocity precursor wind. At the poles, a cold thin shell behind the inward shock, and a hotter and thicker region behind the outward shock are formed. This difference is due to the radiative cooling of the shocked material behind both shocks (see González et al. 2004a). We find that for the great eruption, the momentum flux is dominated by the material expelled during the eruptive event (that is, the pre-outburst wind to the great eruption momentum ratio, $\dot{m}_0 v_0 / \dot{m}_{ge} v_{ge} \ll 1$ (where \dot{m}_{ge} and v_{ge} are the mass loss rate and the wind velocity during the eruption, respectively), so that the pre-outburst wind has a minor effect on the kinematics and morphology of the bipolar lobes. Since the mass loss rate during the eruption is more than two orders of magnitude (a factor of 500; see Table 1) larger than that of the pre-outburst wind, the Homunculus retains almost the same degree of asymmetry imprinted in the 1840s event near the star.

We note that the shape and kinematics of the outer expanding shell resembles that of the large Homunculus previously simulated by González et al. (2004a, b), but important differences from these previous models are identified in the embedded structures of Figure 3. In the case of the minor eruptive event, the momentum flux is also dominated by the eruption, but the post-outburst wind has a significant effect on the kinematics and morphology of the inner Homunculus once the low-velocity downstream material is completely incorporated to the layer. González et al. (2006) have shown that this happens at a critical time $t_c = (\Delta t) / (\sigma - 1)$, being Δt ($= 10$ yr) the duration of the eruptive event. Adopting the flow parameters given in § 3.1 ($\sigma \simeq 1.25$; $a = 2.53$ and $b = 0.1$), we obtain $t_c \simeq 39.4$ yr. In Figure 4, we show the behaviour of

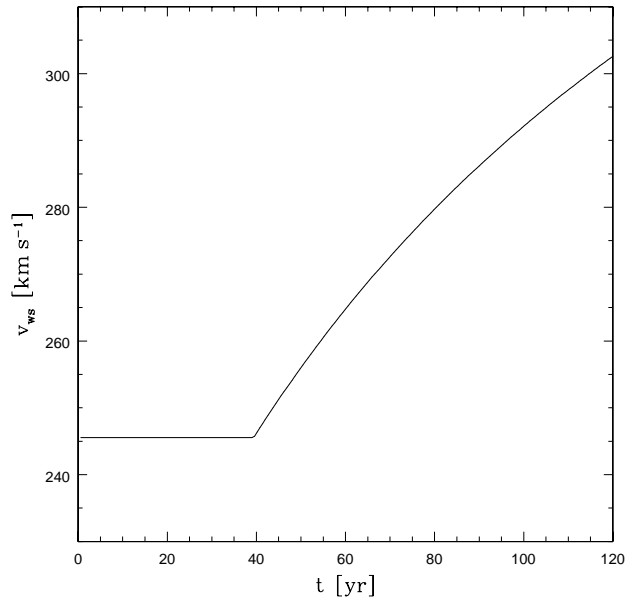


Figure 4. Behaviour of the velocity of the polar caps of the inner Homunculus as a function of time. Initially they move with constant velocity ($\sim 245.55 \text{ km s}^{-1}$). At a critical time $t = 39.4$ yr (when the downstream shock disappears), the caps begin to be accelerated, asymptotically approaching the velocity of the post-outburst wind ($\sim 495.62 \text{ km s}^{-1}$). After 109 yr of evolution (i.e., around the year of 2009) they expand at $\sim 297 \text{ km s}^{-1}$. This value is consistent with the observed current expansion speed of $\sim 250 \text{ km s}^{-1}$ of the little Homunculus (Smith 2005).

the velocity of the polar caps of the inner Homunculus as a function of time. Initially, they move with constant velocity ($\sim 245.55 \text{ km s}^{-1}$; see eq. [3]), until the downstream shock disappears and a one-shock structure stage begins. Later, the polar caps begin to be accelerated, asymptotically approaching the velocity of the post-outburst wind (see also González & Cantó 2002). After 109 yr of evolution (around year 2009), they expand at $\sim 297 \text{ km s}^{-1}$ and are located at a position $r_s \simeq 9.07 \times 10^{16} \text{ cm}$ from the star. At a distance of 2.3 kpc, r_s corresponds to an angular size of ± 2.6 arcsec, which is consistent with the angular extent of roughly ± 2 arcsec (along the major axis) of the inner Homunculus measured by Ishibashi et al. (2003). This is also consistent with the angular size (± 3 arcsec) observed in the simulations.

The inner Homunculus quickly becomes Rayleigh-Taylor unstable (see figure 5) due to the interaction of the low-density fast wind (post-outburst wind) that pushes and accelerates the high-density slow wind (minor eruption). The growth time for this instability can be estimated as follows.

The density of the fast wind at the position of the shock, r_s , is obtained by,

$$\rho_{fw} = \frac{\dot{M}_{fw}}{4\pi v_{fw} r_s^2}, \quad (8)$$

where \dot{M}_{fw} is the mass loss rate of the wind, and v_{fw} is its velocity at r_s . On the other hand, the shock-bounded layer of the slow wind has a surface density σ_{sw} given by,

$$\sigma_{sw} = \frac{M_{sw}}{4\pi r_s^2}, \quad (9)$$

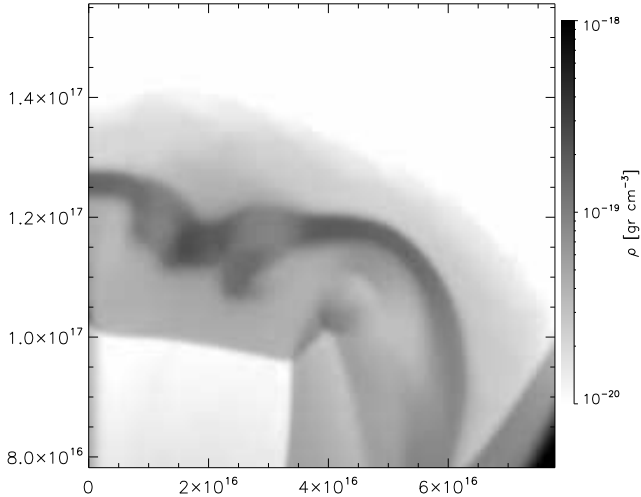


Figure 5. Detail of the density map of Fig. 3, showing the little Homunculus at $t = 119$ yr after the minor eruptive event of η Car (or around the year 2009). The low-density fast wind (post-outburst wind) pushing the high-density slow wind (minor eruption) causes the polar caps of the little Homunculus to become Rayleigh-Taylor unstable.

where $M_{sw} = \dot{M}_{sw} \Delta t$ is the mass in the shock-bounded layer, Δt is the time interval of injection of the slow wind, and \dot{M}_{sw} is its mass loss rate. In the above, we have assumed that the shock-bounded layer is thin.

Initially, the shock-bounded layer (and the slow wind shock) moves with a velocity v_s given by (eq. [3]),

$$v_s = \sigma v_{sw} \quad (10)$$

where v_{sw} is the velocity of the slow wind. In the shock reference frame, the fast wind moves with velocity $v = v_{fw} - v_s$, and thus exerts a hydrodynamical pressure $\rho_{fw} v^2$ on the shock-bounded layer. This layer will therefore, experience an acceleration $a_s = \rho_{fw} v^2 / \sigma_{sw}$. Taking the values of the mass loss rates and wind velocities from Table 1, we obtain a value for the acceleration experienced by the layer of $a_s = 3.96 \times 10^{-3} \text{ cm s}^{-2}$.

The dispersion relation for the Rayleigh-Taylor (RT) instability is calculated by,

$$\omega_k = -\frac{\rho_2 - \rho_1}{\rho_2 + \rho_1} gk, \quad (11)$$

where $\rho_2 > \rho_1$ are the densities of the fluid layers, g is the acceleration, and k is a wave number. We identify $\rho_2 = \rho_{sw}$, $\rho_1 = \rho_{fw}$ and $g = a_s$. Considering that the growth rate for the RT instability is largest for the shortest wavelengths, we adopt the minimum resolved wavelength as 3 times the resolution of our simulation, $\lambda_{RT} = 1.17 \times 10^{15} \text{ cm}$. With $\rho_{fw} = 10^{-18} \text{ g cm}^{-3}$ and $\rho_{sw} = 2 \times 10^{-17} \text{ g cm}^{-3}$, the RT instability grows in about one year, in agreement with the simulations.

In Figure 6, we show that our model of interacting non-spherical winds can explain the formation of the large and little Homunculi. From the simulations, we have found an

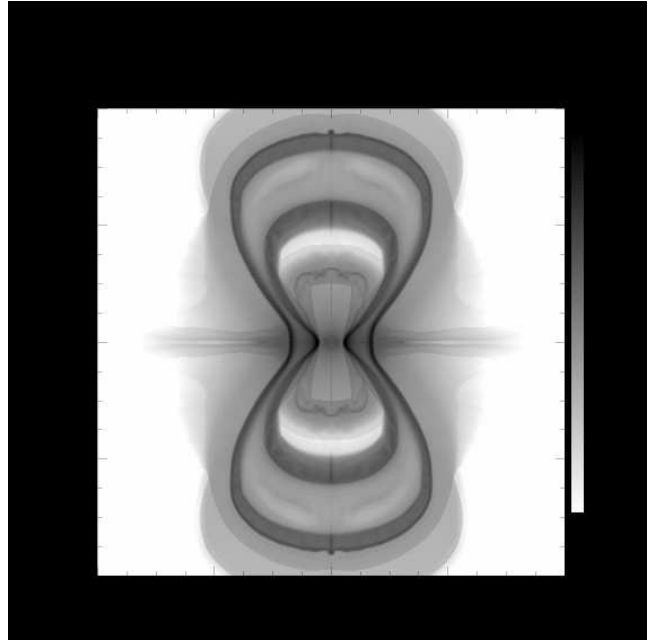


Figure 6. Present-day structure of the η Car nebulae. The inner and outer Homunculus and a tenuous equatorial skirt are depicted. A thick dense layer between both Homunculi is also observed.

appropriate combination of the flow parameters (which control the degree of asymmetry) that best matches the kinematic structure of the thin outer shell of H_2 observed by Smith (2006). In contrast with our previous models of η Car (González et al. 2004a,b) in which we observed a hollow nebula, it is noteworthy that the new numerical experiments show a thicker layer (with a density between $\simeq 10^{-20} \text{ g cm}^{-3}$ and $10^{-18} \text{ g cm}^{-3}$ along the symmetry axis) partially filling the interior of the lobes of the large Homunculus. It may be related with the inner skin of [Fe II] emission detected by Smith (2006).

On the other hand, as in the previous work, the high-velocity ejections at equator, which arise from the impact of the external Homunculus on the shock front of the pre-eruptive wind, resemble the observed equatorial skirt of η Car. At a time $t \simeq 100$ yr after the great eruption turn-on, the impact at low latitudes occurs producing a hot ($T \simeq 10^7 \text{ K}$), tenuous ($\rho \simeq 10^{-18} \text{ g cm}^{-3}$) structure. This structure is accelerated, reaching an expansion velocity of $\sim 1000 \text{ km s}^{-1}$ and produces fast ejected material that could be related to the observed material confined to the equatorial plane of η Car. The gas is concentrated to the equator by the impact of the two shock fronts, and then it flows into an environment of decaying pressure. Why are these equatorial features moving faster and what accelerate them in our simulations are still open issues which we will attend in a forthcoming paper. This effect has been also addressed in González et al. (2004a,b) and it is probably connected with a *nozzle* problem. As can be seen in the simulations (Figs. 3 and 6), the equatorial ejection has some resemblance with a supersonic flow through a tube of varying cross-sectional area (the problem of the *de Laval nozzle*). At supersonic

speeds, an increase in velocity is expected when the area of the nozzle increases, such as our models show.¹

4 DISCUSSION AND CONCLUSIONS

In this article, we carried out high-resolution two-dimensional gasdynamic simulations of the dramatic outbursts suffered by the star η Car during the 1800s, the larger of which occurred in the 1840s and resulted in the formation of the large Homunculus nebula and the smaller one in the 1890s created the inner little Homunculus. During these events, the parameters of the η Car wind may have drastically changed in short periods of time. In contrast with the great eruption (where both the mass loss rate and the ejection velocity were suddenly increased), during the minor event of the 1890s (much fainter and of shorter duration than the 1840s event) the mass loss rate was enhanced, but the wind velocity diminished compared with the normal η Car wind.

Considering a simplified interacting stellar wind scenario, we could explain the shape and the observed expansion speed (as a function of latitude) of the large Homunculus. In addition, our numerical models show that the little Homunculus is formed at the *end* of the 1890s eruption, when the post-outburst η Car wind collides with the eruptive outflow. Important differences with regard to our previous models of the η Car nebula (González et al. 2004a,b) have been obtained. In González et al. (2004a,b), we assumed that the impact between the 1890 outburst and the pre-outburst wind was the cause of the development of the little Homunculus nebula. As a matter of fact, although the momentum flux is dominated by the 1890s eruption, the post-outburst wind has an important effect on the kinematics and morphology of the little Homunculus as it causes the complete deposit of the material expelled during the eruption into the polar caps. At this time, the powerful stellar wind accelerates the inner Homunculus material so that it asymptotically reaches the velocity of the post-outburst wind. Due to Rayleigh-Taylor instabilities generated by the low-density fast wind pushing the high-density slow wind, the polar caps of the inner Homunculus quickly develop filamentary structuring (Fig. 5) that shows some resemblance with the observed spatial structures in the polar lobes of the little Homunculus by Smith (2005) that suggest that it is not perfectly homologous to the larger Homunculus nebula.

Also, in contrast with the previous models of η Car (González et al. 2004a,b), it is noteworthy that in the present numerical modeling the interior cavity between the Homunculi is partially filled by material that is expelled during the decades following the end of the 1840s great eruption, rather than being almost empty. This agrees with the observed double-shell structure observed in the polar lobes by

Smith (2006), consisting of a thin outer H₂ skin (which contains most of the material of the nebula) and a thicker [Fe II] layer with a more irregular spatial distribution.

As in the previous models (González et al. 2004a,b), the present results show the formation of an equatorial outflow with both low and high velocity features. These are probably related to the equatorial skirt of η Car. We note however, although it has been predicted that the observed skirt might be associated with the two outbursts (e.g. Davidson et al. 2001), our simulations indicate that only the great eruption contributes to its formation.

A final remark is in order. One could ask whether one can learn about the progenitor of Eta Car from the assumed mass loss history or what can cause such sharp changes in the mass loss rate and speed, without affecting the general shape of the Homunculi. As stressed in González et al. (2004a,b), these questions are very probably connected with Eta Car being a binary star system and the nature of the interaction between the main and companion stars. In this work, however, we have focussed in the formation and dynamical evolution of the shock structures associated to the large and little Homunculi given the parameters (terminal velocity, mass-loss rate and/or density) of the different wind phases, without addressing the inner mechanism that first triggered it or its variability at the much smaller scales of the central source of Eta Car. The orbit of the secondary star, for instance, has apoastro and periastro distances of ~ 14 AU and ~ 3 AU, respectively, while in our simulations, the outflows are injected at much greater distances (10^{16} cm). A detail study univocally connecting both the inner source scales and the outer scales was, therefore, out of the scope of the present study. Nonetheless, there have been some first efforts in this direction (e.g., Soker 2001 ; Falceta-Gonçalves & Abraham 2009) that should be further explored in the future.

ACKNOWLEDGMENTS

The work of RFG and AVC was supported by the DGAPA (UNAM) grant IN 117708. GCG thanks DGAPA (UNAM) grant IN 106809 and CONACyT grant 50402-F. AR, JC, and PFV acknowledge financial support by CONACyT grants 46828-F and 61547. EMGDP has been partially supported by the Brazilian Foundations FAPESP (2006/50654-3) and CNPq grants. The authors have benefited from elucidating conversations and comments from Z. Abraham and M.A. de Avillez. The authors also thank the useful comments of the referee Noam Soker.

REFERENCES

¹ We notice that the effect described here is distinct from the one discussed, e.g., in Akashi & Soker (2008). These authors claim the presence of jets (or collimated fast winds) launched by the central star (or by a companion) to explain the presence of an expanding disk and then relate its acceleration to compression of the material in the equatorial plane by the two lobes.

- Akashi, M., Soker, N. 2008, MNRAS, 391, 1063
- Cantó, J., González, R.F., Raga, A.C., de Gouveia Dal Pino, E.M., Lara, A., González-Esparza, J.A., 2005, MNRAS, 357, 572
- Cantó, J., Raga, A.C., D'Alessio, P., 2000, MNRAS, 313, 656
- Corcoran, M.F., Ishibashi, K., Swank, J.H., Petre, R., 2001, ApJ, 547, 1034

- Currie, D.G., Dowling, D.M., Shaya, E.J., 1996, AJ, 112, 1115
- Damineli, A., 1996, ApJ Lett., 460, L49
- Damineli, A., Conti, P.S., Lopes, D.F., 1997, NewA, 2, 107
- Davidson, K., 1987, ApJ, 317, 760
- Davidson, K., Humphreys, R.M., 1997, ARA&A, 35, 1
- Davidson, K., Smith, N., Gull, T.R., Ishibashi, K., Hillier, D.J., 2001, AJ, 121, 1569
- Duncan, R.A., White, S.M. 2003, MNRAS, 338, 425
- Dwarkadas, V.V., Balick, B. 1998, AJ, 116, 829
- Falceta-Gonçalves, D., Abraham, Z., 2009, MNRAS, 399, 1441
- Frank, A., Balick, B., Davidson, K., 1995, ApJ Lett., 441, L77
- Frank, A., Ryu, D., Davidson, K., 1998, ApJ, 500, 291
- González, R.F., Cantó, J., 2002, ApJ, 580, 459
- González, R.F., de Gouveia Dal Pino, E.M., Raga, A.C., Velázquez, P.F., 2004a, ApJ Lett., 600, L59
- González, R.F., de Gouveia Dal Pino, E.M., Raga, A.C., Velázquez, P.F., 2004b, ApJ, 616, 976
- González, R.F., Montes, G., Cantó, J., Loinard, L., 2006, MNRAS, 373, 391
- Hillier, D.J., Allen, D.A., 1992, A&A, 262, 153
- Humphreys, R.M., Davidson, K., Smith, N., 1999, PASP, 111, 1124
- Humphreys, R.M., Davidson, K., 1994, PASP, 106, 1025
- Icke, V. 1988, A&A, 202, 177
- Ishibashi, K., et al., 2003, AJ, 125, 3222
- Langer, N., García-Segura, G., Mac Low, M., 1999, ApJ Lett., 520, L49
- Le Sueur, A., 1870, Proc. Roy. Soc., 18, 245
- Matt, S., Balick, B., 2004, ApJ, 615, 921
- Morse, J.A., Davidson, K., Bally, J., Ebbets, D., Balick, B., Frank, A., 1998, AJ, 116, 2443
- Pittard, J.M., Corcoran, M.F., 2002, A&A, 383, 636
- Raga, A.C., Cantó, J., Binette, L., Calvet, N., 1990, ApJ, 364, 601
- Raga, A.C., de Gouveia Dal Pino, E.M., Noriega-Crespo, A., Mininni, P.D., Velázquez, P.F., 2002, A&A, 392, 267
- Raga, A.C., Navarro-González, R., Villagrán-Muniz, M., 2000, Rev. Mex. Astro. Astrofis., 36, 67
- Retallack, D.S., 1983, MNRAS, 204, 669
- Seward, F.D., Butt, Y.M., Karovska, B.M., Prestwich, A., Schlegel, E.M., 2001, ApJ, 553, 832
- Smith, N., 2005, MNRAS, 357, 1330
- Smith, N., 2006, ApJ, 644, 1151
- Smith, N., Gehrz, R.D., 1998, AJ, 116, 823
- Smith, N., Gehrz, R.D., Hinz, P.M., Hoffmann, W.F., Hora, J.L., Mamajek, E.E., Meyer, M.R., 2003a, AJ, 125, 1458
- Smith, N., Davidson, K., Gull, T.R., Ishibashi, K., Hillier, D.J., 2003b, ApJ, 586, 432
- Smith, N., Morse, J.A., 2004, ApJ, 605, 854
- Soker, N., 2001, MNRAS, 325, 584
- Soker, N., 2004, ApJ, 612, 1060
- Van Leer, B., 1982, ICASE Rep. 82-30 (Washington NASA)
- Walborn, N.R., 1976, ApJ, 204, L17
- Walborn, N.R., Blanco, B.M., Thackeray, A.D., 1978, ApJ, 219, 498
- Walborn, N.R., Liller, M.H., 1977, ApJ, 211, 181
- Weis, K., 2005, *The Fate of the Most Massive Stars*, ASP Conference Series, Vol. 332
- Weis, K., Duschl, W.J., Bomans, D.J., 2001, A&A, 367, 566
- White, S.M., Duncan, R.A., Lim, J., Nelson, G.J., Drake, S.A., Kundu, M.R., 1994, ApJ, 429, 380
- Whitney, C.A. 1952, Harvard Bull., No. 921, p. 8